

1 Fire performance of charring closed-cell polymeric insulation materials:
2 polyisocyanurate and phenolic foam

3 Juan P. Hidalgo^{a,b1}, José L. Torero^b, Stephen Welch^a

4 ^a School of Engineering, The University of Edinburgh, Edinburgh, EH9 3JL, UK

5 ^b School of Civil Engineering, The University of Queensland, Brisbane St Lucia, QLD 4072, Australia

6 Abstract

7 Results are presented from two series of ad-hoc experimental programmes using the Cone Calorimeter to
8 investigate the burning behaviour of charring closed-cell polymeric insulation materials, specifically
9 polyisocyanurate (PIR) and phenolic (PF) foams. These insulation materials are widely used in the
10 construction industry due to their relatively low thermal conductivity. However, they are combustible in
11 nature; therefore, their fire performance needs to be carefully studied, and characterisation of their thermal
12 degradation and burning behaviour is required in support of performance-based approaches for fire safety
13 design. The first series of experiments was used to examine the flaming and smouldering of the char from
14 PIR and PF. The peak heat release rate per unit area was within the range of 120 to 170 kW·m⁻² for PIR
15 and 80 to 140 kW·m⁻² for PF. The effective heat of combustion during flaming was within the range of 13
16 to 16 kJ·g⁻¹ for PIR and around 16 kJ·g⁻¹ for PF, while the CO/CO₂ ratio was within 0.05 to 0.10 for PIR
17 and 0.025 to 0.05 for PF. The second experimental programme served to map the thermal degradation
18 processes of pyrolysis and oxidation in relation to temperature measurements within the solid-phase under
19 constant levels of nominal irradiation. Both programmes showed that surface regression due to smouldering
20 was more significant for PF than PIR under the same heat exposure conditions, essentially because of the
21 different degree of overlap in pyrolysis and oxidation reactions. The smouldering of the char was found to
22 self-extinguish after removal of the external heat source.

23 Keywords

24 Insulation materials; Charring foams; Pyrolysis; Smouldering; Combustion; Performance-based design

25 Nomenclature

$E_{CO \rightarrow CO_2}$ heat release per mass unit of oxygen consumed for the combustion of carbon monoxide (J·g⁻¹)

¹ Corresponding author: j.hidalgo@uq.edu.au

E_{O_2}	heat release per mass unit of oxygen consumed ($J \cdot g^{-1}$)
ΔH_c	heat of combustion ($J \cdot g^{-1}$)
m	mass ($g \cdot s^{-1}$)
\bar{m}	normalised mass (-)
\dot{m}	mass flow rate ($g \cdot s^{-1}$)
\dot{Q}	heat release rate (W)
t	time (s)
T	temperature (K or $^{\circ}C$)
X	volume fraction ($mol \cdot mol^{-1}$)
\dot{V}	volumetric flow ($m^3 \cdot s^{-1}$)

Greek letters

γ	volumetric expansion factor (-)
ϕ	oxygen depletion factor (-)

Subscripts

0	Initial
<i>air</i>	of air
<i>eff</i>	Effective
<i>end</i>	of the end duration of the test
<i>e</i>	of the exhaust or extraction
<i>i</i>	of the species i
<i>loss</i>	of total loss from the sample
<i>s</i>	loss from the sample

Acronyms

CDG	carbon dioxide generation calorimetry
DTG	differential thermogravimetric analysis
HRR	heat release rate
HRRPUA	heat release rate per unit area
OC	oxygen consumption calorimetry
PIR	closed-cell rigid polyisocyanurate foam
PF	closed-cell rigid phenolic foam
TC	Thermocouple
TGA	thermogravimetric analysis

26 1. Introduction

27 Stringent requirements for energy efficiency are driving a trend towards the more widespread use of
 28 insulation materials in the built environment. Several types of insulation materials, which are able to meet

29 the multiple design criteria often required for buildings, can be found in the market. A typical classification
30 for insulation materials in the European market, proposed by *Papadopoulos et al.* [1], distinguishes four
31 main groups: (1) inorganic materials such as foams or fibrous materials, (2) organic materials such as
32 expanded foams or fibrous materials, (3) combined materials, and (4) new technology materials. Expanded
33 organic foams such as closed-cell rigid polyisocyanurate (PIR) and phenolic foam (PF) are common
34 combustible insulation materials that are increasingly being used for the design of energy-efficient buildings
35 due to their relatively low thermal conductivity, low density, good durability and ease of installation [2].
36 These factors, in conjunction with the requirement for lower thermal transmittances in building assemblies
37 [3], lead to these materials increasingly being a preferred option for design.

38 1.1. Fire hazards from combustible insulation

39 The increase in production and extended usage of combustible materials in buildings such as closed-
40 cell cellular polymers has recently given rise to several concerns in the fire safety community [4, 5]. This
41 is however not a new problem, and many aspects have already been addressed by several authors and
42 institutions in the past [6]. Indeed, in order to identify the potential fire hazards to life safety from insulation
43 materials in buildings, numerous authors have extensively studied the fire performance of different types
44 of insulation under different approaches [6-24]. The biggest concern, represented as the flammability and
45 energy release, has classically been addressed using bench-scale experimentation [13-22], e.g. determining
46 the Limiting Oxygen Index (LOI) according to ASTM D2863 [27] and assessing ignition properties, heat
47 release and flame spread by using the Cone Calorimeter [28] or the LIFT apparatus [29]. During recent
48 decades, the fire performance of these materials has been improved by applying flame retardancy
49 techniques, i.e. promoting charring behaviour and endothermic reactions in the solid phase, which is
50 typically researched at material scale using thermogravimetry [7-9]. The generation of toxic species due to
51 the combustion and pyrolysis of these plastics has also been raised as a potentially significant concern, and
52 several authors have studied the toxicity of emissions from insulation materials commonly used in buildings
53 [10-12].

54 While most of this work has clearly served to rate the hazard from insulation products under specific
55 testing scenarios, several authors highlight that the extrapolation of the performance observed from small-
56 scale testing is hardly applicable to larger scale due to the combination of complex phenomena [23-26].
57 Although significant efforts are constantly made to reduce the flammability/combustibility of these
58 materials, there is potential for confusion from the belief that the risk associated with these hazards can be
59 effectively mitigated by obtaining better ratings from standard testing. Harmonisation of standardised
60 testing is intended to offer a plausible representation of the fire hazards from construction products. Yet,

61 quantification of the risks associated with the use combustible insulation in buildings remains as a
62 significant challenge for practitioners.

63 1.2. Design tools to quantify the risk from combustible insulation

64 Recently, new methodologies for the fire safe design of insulation systems have been proposed based
65 on their material behaviour under severe conditions of heat exposure [30]. The methodology proposed by
66 *Hidalgo et al. (2015)* considers the mitigation of the fire hazard from combustible insulation materials by
67 designing suitable thermal barriers that control the onset of pyrolysis [30, 31], i.e. delaying the onset of
68 hazard generation. Previous work demonstrated that the onset of hazard could be conservatively defined as
69 a ‘critical temperature’ [32]. For charring foams, the ‘critical temperature’ was defined as the temperature
70 at which the peak of the main pyrolysis reaction is obtained by differential thermogravimetric analyses
71 (DTG) at sufficiently low heating rates and under non-oxidative atmospheres.

72 The proposed methodology represents a conservative approach for the quantitative fire safe design of
73 construction systems including insulation materials; i.e. a framework by which the risk can be quantified.
74 Nevertheless, additional models are required by practitioners and regulatory bodies if quantification of the
75 evolution of hazard after the onset of pyrolysis is to be understood [33], i.e. potential heat release
76 contribution and generation of toxic species from the insulation. The quantification of these hazards is
77 determined by the terms (1) production rate of pyrolysis gases, (2) heat of combustion from pyrolysis gases
78 and (3) gas species generated by the pyrolysis and combustion. In order to be able to quantify these
79 parameters and propose a model for performance-based design, a thorough understanding of the material
80 behaviour under conditions of heat exposure is required. **This study aims at achieving a thorough
81 understanding of the material behaviour beyond standard testing and parameters, thus identifying the
82 underlying processes that govern those issues, i.e. the thermal degradation and thermal evolution of the
83 condensed phase at a relevant scale.**

84 1.3. Research significance and objectives

85 In previous work, we presented studies on flammability properties from PIR and PF, as well as their
86 thermal decomposition processes at a material scale by thermogravimetry [32]. The purpose of that work
87 was to determine parameters for the proposed performance-based design methodology [30]. Values of
88 ‘critical temperature’ established previously, which represent the onset of hazard (pyrolysis), correspond to
89 300 – 370 °C for rigid PIR insulation and 425 °C for the specific phenolic foam studied [32]. The present
90 work explores the fire performance of these materials based on their burning behaviour. Variables such as
91 the heat of combustion, emissions of carbon monoxide (CO) and carbon dioxide (CO₂) and consumption of
92 oxygen (O₂) from the combustion are assessed. Thus, the information presented here aims to provide

93 relevant data for the development and application of models capable of predicting the production rate of
94 energy, pyrolysis, and combustion products under different scenarios.

95 Then, the scope of the work presented herein is to present an original methodology to assess the fire
96 performance of representative samples of two common commercial rigid closed-cell plastic insulation
97 materials (polyisocyanurate and phenolic foam). This work explores which phenomena should be
98 considered for the development and application of models that can quantify their burning hazard. In order
99 to achieve this, the following goals are pursued:

- 100 - Macroscopic analysis of the fire performance of these foams by studying heat release rate, mass
101 loss, and gas emissions from Cone Calorimeter ad-hoc experiments.
- 102 - Mapping of the thermal degradation processes in relation to temperature measurements within the
103 solid-phase, correlating the evolution of the thermal profile experienced by the material to results
104 obtained by thermogravimetric analyses presented elsewhere [32].

105 The present work is vital for the further development of engineering tools that could assist
106 performance-based designs of building assemblies including combustible insulation. As noted by *Hidalgo*
107 *et al.* [30], whereas the current regulatory fire safety frameworks in the EU [34, 35] do not provide a suitable
108 approach for insulation materials, further instrumentation and inclusion of quantitative approaches could
109 complement current standardised testing practices. This approach would help to provide a better
110 understanding and quantification of the fire hazards from insulation materials.

111 It should be noted that the final fire performance of plastic foams such as PIR and PF strongly depend
112 on the chemical composition and manufacturing process [36]; e.g. content of isocyanurate linkages and
113 type of isocyanate-reactive component for PIR, or degree of reticulation for phenolic foams. This
114 information is however largely inaccessible to the public. Since the purpose of this work is to establish a
115 methodology that allows for a comprehensive analysis of phenomena relevant to the eventual fire
116 performance characterisation, three current commercially available types of PIR from different
117 manufacturers were selected. These products are certified by their manufacturers to correspond to
118 isocyanurate-based foams (PIR) rather than urethane-based foams (PUR). Only one phenolic foam product
119 was selected aiming at a performance comparison with respect to PIR foams; previous thermogravimetric
120 studies have shown essential differences between these products [32].

121 2. Experimental programme description

122 The experimental programme designed to achieve the objectives noted above was based on the use of
123 the Cone Calorimeter apparatus [28], as two different series of ad-hoc experiments:

124 (1) Piloted experiments and transferring the heat to the sample by radiation from the cone, as presented
125 for the flammability experiments on insulation materials presented elsewhere [32]. The main
126 measurements consisted of mass loss and gas species such as oxygen, carbon dioxide and carbon
127 monoxide, supported by visual observations.

128 (2) Non-piloted experiments and transferring the heat to the sample by radiation from the cone. The
129 main measurements consisted of gas species and temperature measurements within the samples,
130 supported by visual observations.

131 2.1. Materials

132 The studied insulation materials comprised three types of rigid polyisocyanurate foam (hereby
133 referred as PIRa, PIRb and PIRc, respectively) and one type of phenolic foam (PF). These thermoset plastics
134 are manufactured as rigid closed-cell polymers by blowing a gas through the entire structure of the foam.
135 At present, the blowing agents mainly utilised are n-Pentane, iso-Pentane, cyclo-Pentane and various
136 hydrofluorocarbons that have zero ozone depleting potential [37].

137 Three different PIR foams from various suppliers were selected to assess the difference in their
138 performance. Polyisocyanurate, which is manufactured based on the mix of an organic isocyanate
139 component and an isocyanate-reactive component, is known to present different possible formulations
140 depending on the isocyanate-reactive component used, which determines its thermal stability [8]. Results
141 in further sections show that the characteristic fire performance from the three foams was similar. Therefore,
142 for studying phenolic foam, only one product was selected with the intention to assess its characteristic
143 performance with respect to PIR foam.

144 These materials are often supplied as rigid boards with a protective layer on the surface, which is
145 expected to have some impact on the observed performance during the tests. For the products studied herein,
146 the protective layer corresponds to a low emissivity composite aluminium foil/paper facing. In order to
147 examine this, samples with and without protective layer were tested. Nevertheless, it should be noted that
148 since this work mainly pursued the characterisation of the material, rather than the product to specific testing
149 methods, the effect of the protective layer must be addressed carefully. Samples with a surface area of 90
150 mm by 90 mm and 100 mm thick were tested in the two series of experiments. Samples with the protective
151 layer removed are shown in Figure 1.

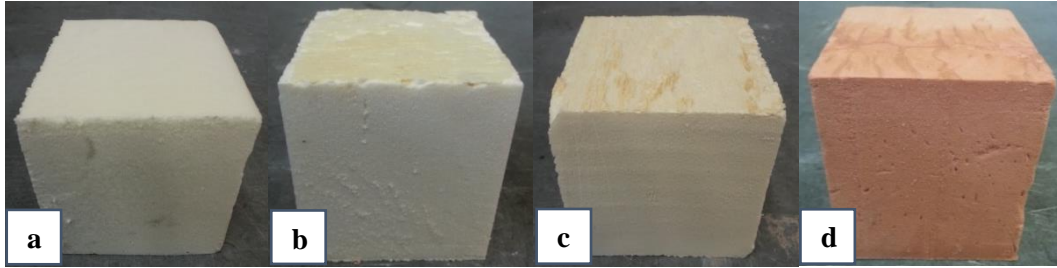


Figure 1. Samples of insulation materials before testing.

(a) PIRa (b) PIRb (c) PIRc (d) PF.

152
153
154

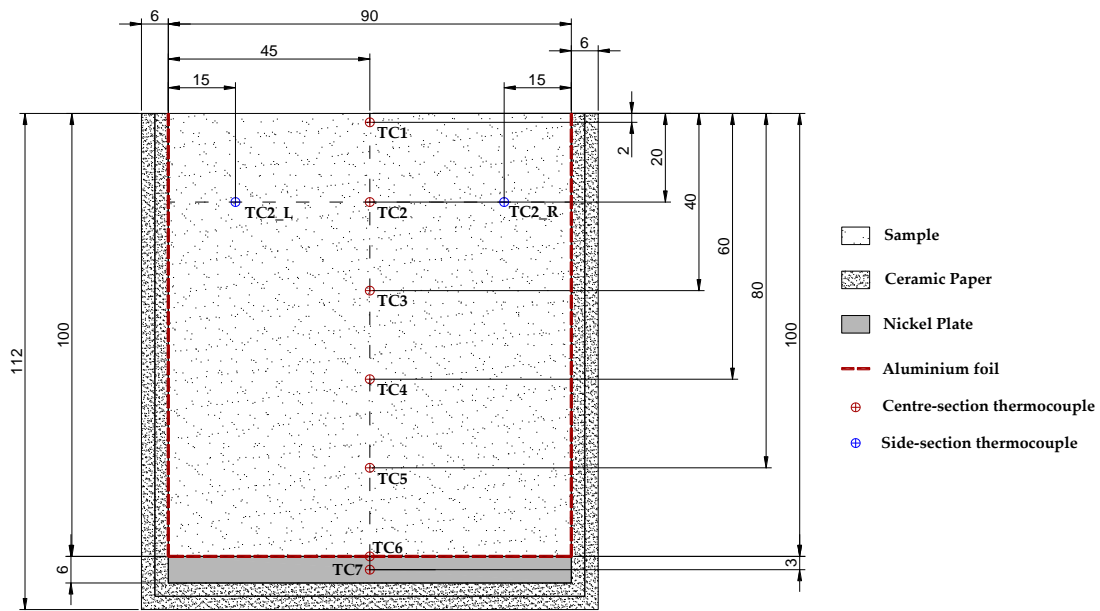
2.2. Set-up #1: Piloted experiments with the heat transferred by radiation

155 The set-up of these experiments is detailed elsewhere [32], the results of which are complementary to
156 those presented here. In the previous publication, the measurements were used to assess the critical
157 temperature and thermal inertia of several insulation materials for a performance-based methodology.
158 **Temperature measurements were not taken for this experimental programme.** The results presented in
159 following sections will rather focus on heat release rate, mass loss, heat of combustion and gas emissions.
160 These provide an assessment of the burning behaviour of these foams with no protective layer, thus a
161 characterisation of the material rather than the product.
162

2.3. Set-up #2: Non-piloted experiments with the heat transferred by radiation

163 For these experiments, samples were wrapped with aluminium foil at the bottom and lateral sides, with
164 a 6 mm Nickel 200 block at the bottom, and altogether wrapped in two 3 mm thick layers of ceramic
165 insulation paper. The aluminium foil was mainly used to prevent air penetration in the sample from the
166 sides and only allow it from the top. From a heat transfer perspective, the foil is transparent for the
167 conducted heat due to its low thickness and high thermal diffusivity, thus acting as a thermally thin material.
168 The two layers of ceramic paper were used in order to reduce the thermal gradients on the surface of the
169 sample sides. It should be noted that an adiabatic boundary condition at the sides will always be unattainable
170 with this set-up since the conductivity of the ceramic paper is higher than the materials tested². A schematic
171 drawing of the conceptual set-up and the real set-up are shown in Figure 2 and Figure 3, respectively.
172

² Thermal conductivity of ceramic paper: 0.08 and 0.11 W·m⁻¹·K⁻¹ at 600 and 800°C, respectively.



173

174

Figure 2. Schematics of sample preparation for the set-up #2.

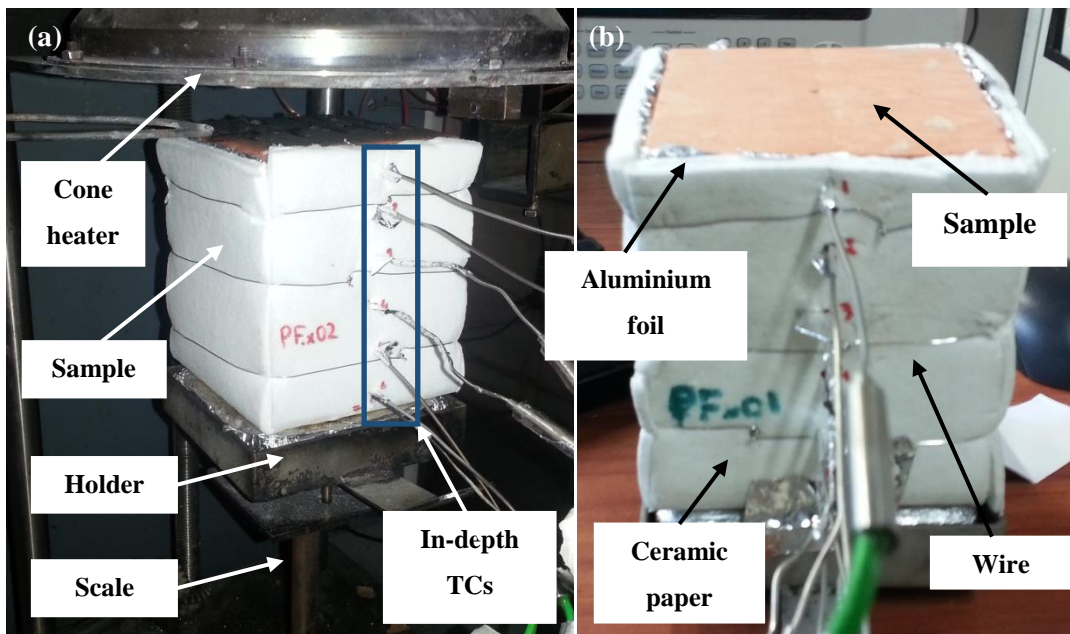
175

176

177

178

It should be noted that this set-up was used to provide relevant and reliable results that could facilitate future modelling tasks. Thus, the characterisation of the boundary condition at the back face of the material is achieved by using the 6 mm Nickel 200 plate at the bottom of the samples. This approach was described by *Carvel et al.* [38], who recommended the use of a heat sink for material characterisation purposes.



179

180

Figure 3. (a) Sample during testing (b) Sample prepared before testing.

181

182

As for the boundary condition at the exposed surface, several values of irradiation from the radiant heater were used. The heat fluxes were selected in such a way that mapping of the different thermal

183 degradation processes was highlighted. The minimum heat flux for each material was defined as a thermal
 184 exposure that did not trigger the onset of pyrolysis after reaching thermal equilibrium. Specific values of
 185 external heat flux for each material are noted in Table 1.

186 Experiments were performed at least twice in order to verify the repeatability of the results, and for
 187 two different configurations, i.e. with no protective layer and with a non-coloured protective layer attached
 188 to the exposed surface in order to explore different phenomena and thermal behaviour experienced by the
 189 foams.

190 Measurements of temperature were taken within the sample by using 1.5 mm bead K-type
 191 thermocouples. The temperature of the metallic plate at the back was also measured. Thermocouples were
 192 installed at the centre of the section and every 2 mm in-depth and in parallel to the exposed surface with
 193 the intention of reducing the error in the thermocouple measurement, which is a recommended procedure
 194 for materials of particularly low conductivity [39, 40]. The first thermocouple was placed within a range of
 195 2-3 mm from the surface. No temperature correction was considered by the heat losses introduced by the
 196 thermocouple. Additionally, two thermocouples were inserted 30 mm horizontally off the second in-depth
 197 thermocouple for some experiments. This procedure aimed to clarify whether the heat transfer through the
 198 sample was behaving either one-dimensionally or two-dimensionally. The positioning of the thermocouples
 199 is shown in Figure 2. A summary of the conditions for all the performed experiments is presented in Table
 200 1.

201 Gas species such as carbon dioxide, carbon monoxide and oxygen were measured at the apparatus
 202 exhaust duct, which nominal volumetric flow corresponded to $24 \text{ l}\cdot\text{s}^{-1}$. **Mass loss was not measured for this
 203 experimental programme, as the thermocouples would interfere with the measurements.**

204 Table 1. Summary of performed experiments (set-up #2).

Material	Configuration	Incident radiant heat flux range /kW·m ⁻²	Measured parameters
PIRa Manufacturer-claimed density: 31 - 34 kg/m ³ Average measured density: 31.2 ± 0.61 kg/m ³	Nominal sample size: 90 mm x 90 mm x 100 mm Exposed surface: (a) With protective layer (b) Without protective layer Wrapping: 2 layers of ceramic paper + 1 layer of aluminium foil	10, 25, 35 (2 repetitions)	(1) In-depth temperature (2) O ₂ , CO ₂ and CO gas species
PIRb Manufacturer-claimed density: 32 kg/m ³ Average measured density: 33.0 ± 0.71 kg/m ³	Back boundary condition: Nickel 200 plate (6 mm) + Ceramic board (25 mm) Orientation: Horizontal Pilot:	5, 10, 25, 35 (2 repetitions)	

<p>PIRc Manufacturer-claimed density: 30 - 32 kg/m³ Average measured density: 33.5 ± 0.65 kg/m³</p>	No pilot igniter	5, 10, 25, 35 (2 repetitions)	
<p>PF Manufacturer-claimed density: 35 kg/m³ Average measured density: 38.1 ± 1.05 kg/m³</p>		5, 10, 15, 25 (2 repetitions)	

205 3. Analysis methodology

206 The calorimetry approach considered to evaluate the heat release rate (HRR) from the burning of the
207 insulation materials is the species evolution approach based on oxygen consumption (OC) [41]. Oxygen
208 consumption rather than carbon dioxide generation calorimetry (CDG) [42] is used to correlate the HRR
209 due to two main reasons: (1) the desiccation system based on calcium sulphate (*drierite*®) tends to absorb
210 carbon dioxide when anhydrous, thus affecting the shape of the measured curve of carbon dioxide, and (2)
211 the variability of energy coefficients for CDG tends to be larger than OC [44]. Then, the formulation
212 considered for the experiments corresponds to OC calorimetry, noted in Eq. (1), which was originally
213 proposed by *Janssens* [43] and has been revisited by *Biteau* [44]:

$$\dot{Q}_{OC} = \left(E_{O_2} \cdot \phi - (E_{CO \rightarrow CO_2} - E_{O_2}) \cdot \frac{1 - \phi}{2} \cdot \frac{X_{CO}}{X_{O_2}} \right) \cdot \frac{\dot{m}_{ex}}{1 + \phi \cdot (\gamma - 1)} \cdot \frac{M_{O_2}}{M_{air}} \cdot X_{O_2}^0 \quad (1)$$

214 where E_{O_2} and $E_{CO \rightarrow CO_2}$ are the energy released per mass unit of oxygen consumed ($W \cdot g^{-1}$) and per mass
215 unit of oxygen consumed for the combustion of carbon monoxide respectively ($W \cdot g^{-1}$), \dot{m}_e is the mass
216 flow in the exhaust ($g \cdot s^{-1}$), γ is the volumetric expansion factor (-), M_{O_2} and M_{air} are the molecular
217 weight of oxygen and air respectively ($g \cdot mol^{-1}$), and ϕ is the oxygen depletion factor (-).

218 The effective heat of combustion $\Delta H_{c,eff}$ ($J \cdot g^{-1}$) is quantified based on calculations of HRR and
219 experimental mass loss, given by:

$$\Delta H_{c,eff} = \frac{\int_0^{t_{end}} \dot{Q}_{OC}(t) \cdot dt}{m_{loss}} \quad (2)$$

220 where $\dot{Q}_{OC}(t)$ is the heat release rate (W), t_{end} is the end time of the test (s), and m_{loss} is the total mass
221 loss during the test (g). The notation ‘effective’ relates to an average value obtained by the combustion of
222 the material. However, the combustion process for most of these foams is non-uniform, with transition from
223 flaming to smouldering, as will be shown in further sections. Then, if Eq. (2) is applied for the total test
224 time, the obtained values of heat of combustion will represent a lumped value that considers both flaming

225 and smouldering as a single process. The effective heat of combustion from pyrolysis gases for materials
226 that char and experience smouldering is attempted for an arbitrary period up to 200 seconds during the
227 initial flaming combustion. This period is chosen considering the samples exposed to heat fluxes larger than
228 35 kW.m⁻² (refer to Figure 5). Even though a shorter integration time would be more adequate for 25 kW.m⁻²,
229 this would lead to large errors due to the short transient behaviour of the flaming combustion. It should
230 be noted that, whereas this is an arbitrary criterion, the objective is to compare this value to the effective
231 value considering the total time of the test.

232 Mass measurements from the samples are normalised with respect to the initial mass of the sample,
233 m_0 (g), as shown in Eq. (3) below:

$$\bar{m}(t) = \frac{m(t)}{m_0} \quad (3)$$

234 where $\bar{m}(t)$ and $m(t)$ are the normalised mass (-) and measured mass (g), respectively, at any time. As
235 discussed in further sections, the ceramic paper used to prepare the samples is expected to lose mass during
236 the test, thus including an overestimation of the mass loss. This error is estimated as a maximum of 5% of
237 the initial sample mass, which is assessed by running tests at high heat fluxes until almost all the sample is
238 consumed.

239 In order to assess the different thermal degradation processes with respect to temperature
240 measurements, the duration of the tests from experimental set-up #2 was selected in a way such that the
241 maximum thermal gradient could be compared to the residue of the sample. Therefore, samples were cut
242 through their centre-section after the end of the test, and the level of thermal degradation achieved at
243 different depths assessed by visual colourimetry. Additionally, the consistency of these results is correlated
244 with thermogravimetric experiments presented elsewhere [32, 36].

245 4. Results and Discussion

246 4.1. Burning behaviour

247 A summary of the experimental results consisting of mass loss of the samples, heat release rate per
248 unit area (HRRPUA), and gas species correlations for PIRa and PF are presented below. For simplicity, and
249 since the results from the rest of PIR materials are very similar in performance, only results from PIRa are
250 discussed in this section.

251 4.1.1. General observations

252 The three types of PIR were found to behave similarly, with a very fast ignition for every external heat
253 flux larger than the critical. This was followed by a small flame which continued to be reduced until

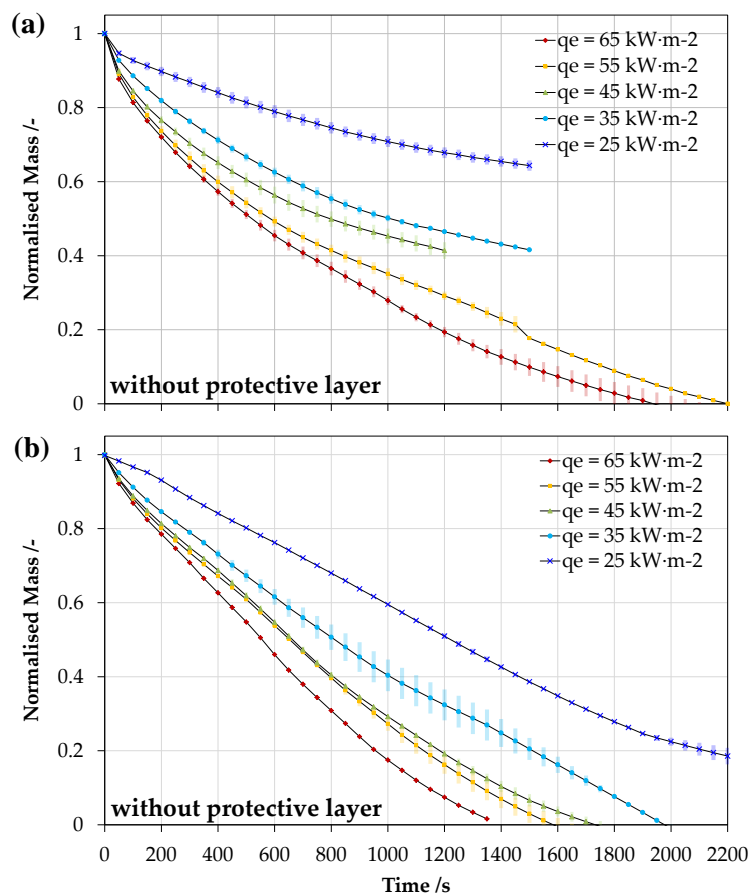
254 intermittent flaming was only observed by the edges of the sample. Polyisocyanurate foam tended to expand
255 slightly at early stages of the heat exposure. After flaming, a black char layer remained which tended to
256 glow if the external heat flux was high. The char at the surface continued to get consumed by oxidation and
257 its thickness started to reduce at different rates depending on the incident radiant heat flux. Flaming at the
258 edges was sporadically observed. The remaining char from PIR was very soft and light. Discolouration of
259 the PIR samples was observed, changing from yellow to orange-brown and finally black colour during the
260 process of thermal degradation. This discolouration is discussed in further sections. It should be noted that
261 the similarity between results from the three types of PIR foams is extensively discussed in [36]. Therefore,
262 herein only main comparative results are presented, and a greater focus is put on PIRa. The reader is referred
263 to [36] for assessing the differences in behaviour for three different PIR foams.

264 Phenolic foam was found to have a similar behaviour to PIR, proceeding to char formation after
265 flaming and to smoulder after flame out at the surface. As shown in previous studies [32], the critical heat
266 flux for ignition is larger than PIR (10-15 kW·m⁻² for PIR, 22 kW·m⁻² for PF); however, its surface
267 regression by smouldering after ignition was shown here to be much faster. Phenolic foam tended to spall
268 and crack very easily during heat exposure and presented a more brittle behaviour. Popping and snapping
269 sounds could be heard during testing. Discolouration was observed, changing from pink-brown to yellow
270 and finally black colour during the process of thermal degradation. This discolouration is discussed in
271 further sections.

272 4.1.2. Normalised mass

273 Figure 4 shows the average curves of normalised mass from two repetitions for PIRa and PF without
274 protective layer at the surface of the samples. For simplicity in the visual assessment of the different
275 evolution of the tests, the mass data is presented as a normalised mass. The normalised mass here refers to
276 the ratio between the mass at any time and the initial mass of the sample before the start of test ($m(t)/m_0$).
277 Therefore, a normalised value of 1 indicates the initial state where the mass of the sample is equal to the
278 initial mass of the sample; a value of 0 indicates that the whole sample has been consumed. For high heat
279 fluxes, samples were tested until near complete consumption of the sample (5% of the mass). Tests at lower
280 heat fluxes (25 – 45 kW·m⁻² for PIR, 25 kW·m⁻² for PF) were interrupted earlier, and the sample was
281 removed as no significant flaming was visible anymore. It should be noted that the sample holder materials
282 also experienced loss of mass; therefore, the normalised measurement includes a maximum error or
283 overestimation of up to a 5%. This explains why the curves presented in Figure 4 reach an absolute
284 normalised mass of 0 in some instances. Due to the unknown mass loss evolution of the sample holder, a
285 correction has not been applied as this would include further uncertainty in the data outputs.

286 The mass loss curves of PIR present a reducing slope throughout the tests, indicating that the pyrolysis
 287 front was moving through thickness leaving a protective char, thus decreasing the rate of pyrolysis.
 288 However, since smouldering was also experienced at the surface of the sample after charring, the change
 289 of slope also includes this phenomenon. Phenolic foam mass loss curves are more linear than the ones
 290 observed for PIR, while PF mass loss is also observed to be larger than PIR for the same heating conditions.
 291 This behaviour is indicative of a more severe consumption of the char at the surface by oxidation
 292 (smouldering) for PF. This is consistent with thermogravimetric experiments presented elsewhere [32],
 293 which indicated that while PIR presents its main pyrolysis (250-350 °C) and oxidation (500-650 °C)
 294 domains in two different temperature regions, the PF main pyrolysis (400-500 °C) and oxidation (480-550
 295 °C) slightly overlap in the same temperature region.

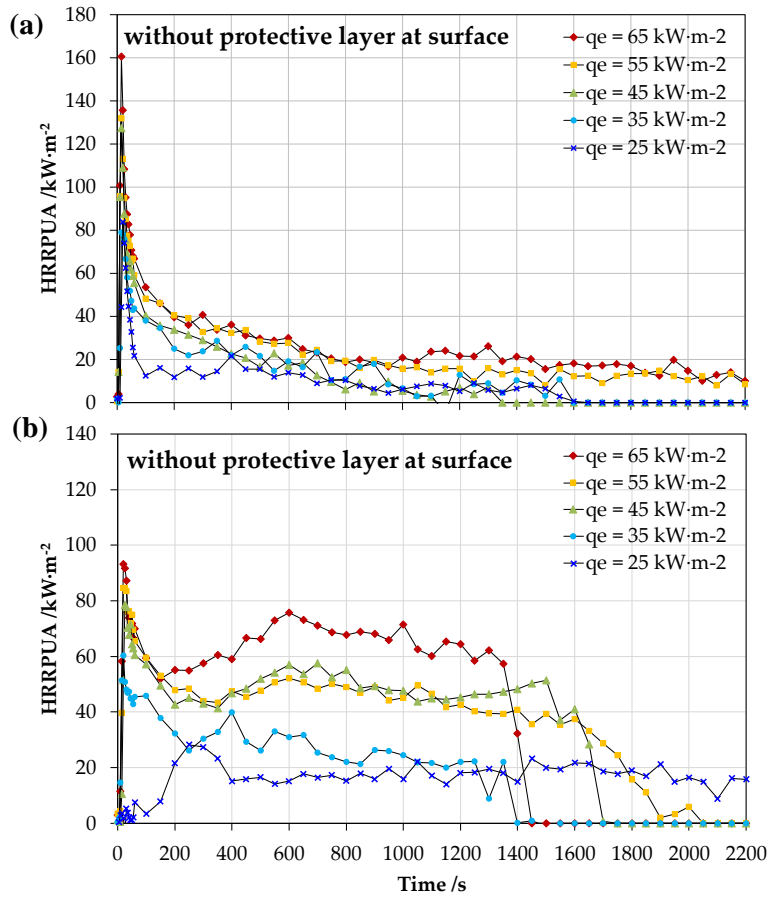


296
 297 Figure 4. Normalised mass ($m(t)/m_0$) of (a) PIRa and (b) PF samples without protective layer at different heat
 298 fluxes. Shading indicates std. dev. from two repetitions.

299 4.1.3. Heat release rate per unit area and effective heat of combustion

300 Figure 5 shows the average heat release rate per unit area (HRRPUA) from two repetitions for PIRa
 301 and PF. In general, PIR samples showed lower HRRPUA than PF throughout the test, except for the peak

302 of HRRPUA. The burning behaviour of PIR and PF showed similar trends, with a large peak of HRRPUA
 303 right after ignition, followed by a progressive decay, which is characteristic of charring materials. This is
 304 generally expected for any PIR. Nevertheless, PF showed a decay of HRRPUA after the first peak, but an
 305 increase for high heat fluxes, which reflects a faster consumption of the char layer.



306
 307 Figure 5. Heat release rate per unit area of 100 mm thick (a) PIRa and (b) PF samples without protective layer
 308 at different external heat fluxes. Average from two repetitions.

309 Table 2 shows the calculated values for the effective heat of combustion for plastic foams PIRa, PIRb,
 310 PIRc, and PF. In general, it is observed that the heat of combustion obtained for the pyrolysis gases
 311 (flaming) is lower than the effective value obtained considering the total test time.

312 Table 2. Calculated effective heat of combustion for plastic foams with no protective layer.

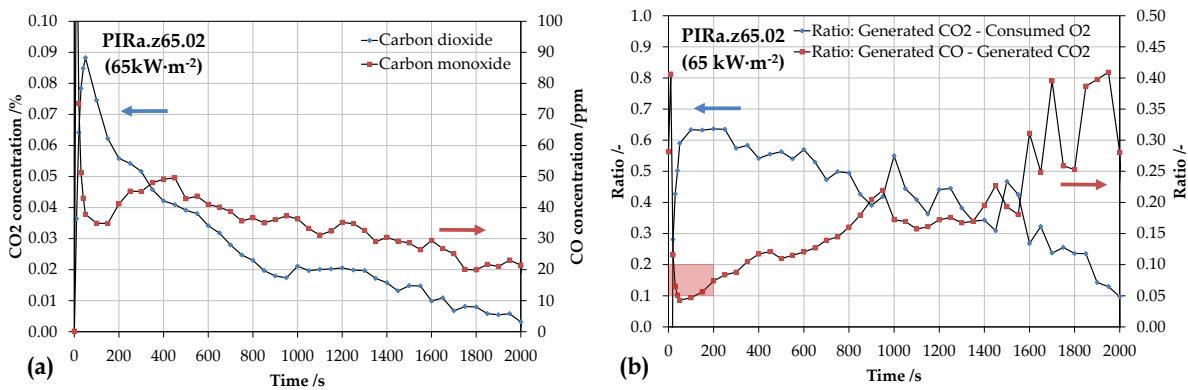
Effective Heat of Combustion / $\text{kJ}\cdot\text{g}^{-1}$				
Integration time	PIRa	PIRb	PIRc	PF
Total test time (t_{end})	19.09 ± 1.99	18.05 ± 2.48	20.52 ± 3.45	20.98 ± 6.01
Up to 200 s (initial flaming)	14.38 ± 0.68	13.22 ± 1.30	16.26 ± 0.84	15.35 ± 0.80

313 4.1.4. Gas species correlations and yields

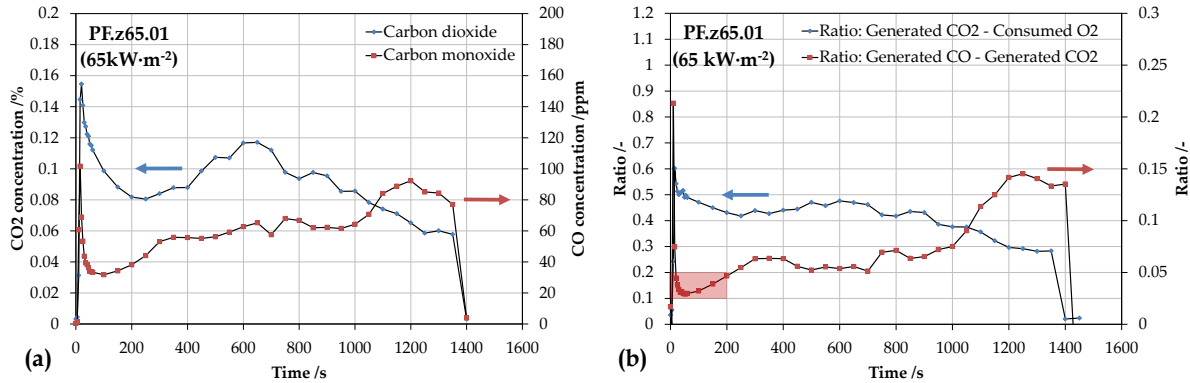
314 Figure 6 shows a selection of gas species correlations of specific tests from PIRa and PF, where high
 315 heat fluxes are selected to represent clearly the different phenomena taking place. The charts on the left
 316 indicate the CO₂ and CO concentrations, while those on the right indicate the ratio of generated CO₂ versus
 317 consumed O₂, and the ratio of generated CO versus CO₂.

318 For PIR and PF, the CO/CO₂ ratio tended to increase greatly during the progress of the test, suggesting
 319 a transition from flaming to smouldering combustion, with both phenomena occurring simultaneously
 320 during some periods of the test. A ratio between 0.05 and 0.10 is observed during flaming combustion (time
 321 before 200 s) for PIR, and between 0.025 and 0.05 for PF; these values are highlighted in Figure 6 and
 322 Figure 7, respectively, with a shading. It is difficult to establish a constant value since a steady-state is not
 323 clearly observed. A clear transition from flaming to smouldering combustion cannot be identified as local
 324 edge effects are present, thus allowing for flaming at the edges while smouldering occurs at the top surface.
 325 The ratio CO/CO₂ continues to increase as the pyrolysis rate and flaming combustion decrease.

326 With regard to the CO₂/O₂ ratio, a short steady-state was initially obtained for PIR, suggesting only
 327 flaming combustion from PIR pyrolysates. This continued to decrease during the period of the test
 328 indicating the transition to a different burning regime, probably with char being consumed by oxidation and
 329 fewer pyrolysis gases being produced due to the spread of the pyrolysis front through thickness. Similar
 330 results were obtained for PF, despite the decrease occurring much earlier, followed by a transition to a
 331 quasi-steady-state. This might be indicative of oxidation of char and flaming of pyrolysis gases occurring
 332 simultaneously. At the final stage of the test, this was reduced again, probably mainly due to the oxidation
 333 of char.



334 Figure 6. (a) CO₂ and CO concentrations and (b) ratios of generated CO₂ vs consumed O₂ and generated O₂
 335 vs generated CO for PIRa at 65 kW·m⁻². The shading denotes the ratio of CO/CO₂ during flaming.
 336
 337



338
 339 Figure 7. (a) CO₂ and CO concentrations and (b) ratios of generated CO₂ vs consumed O₂ and generated O₂
 340 vs generated CO for PF at 65 kW·m⁻². The shading denotes the ratio of CO/CO₂ during flaming.

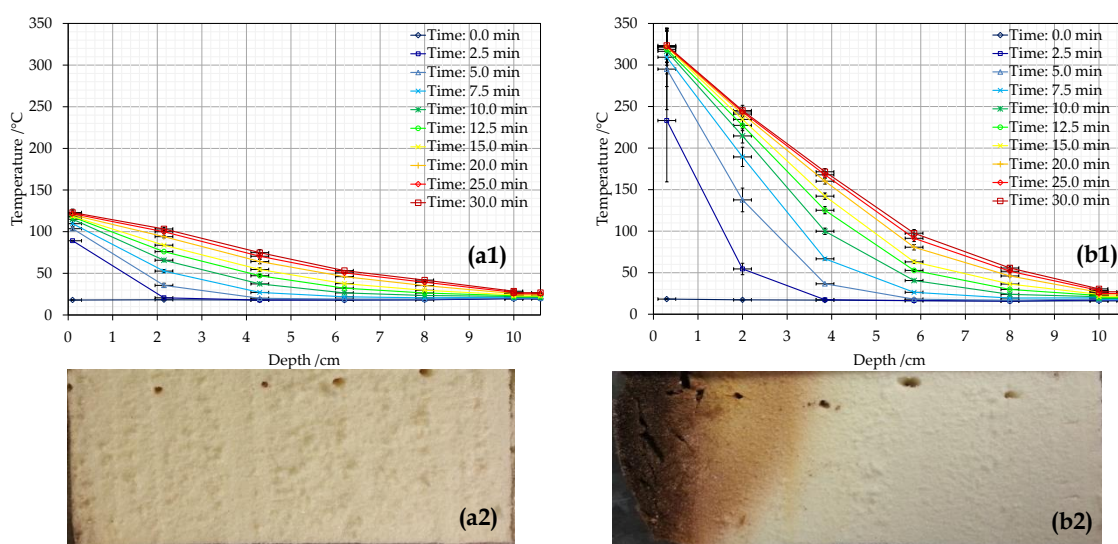
341 4.2. Thermal degradation mapping

342 4.2.1. Isocyanurate-based polyurethane foam (PIR)

343 Figure 8 shows the time history of the in-depth temperature profile for PIRa experiments tested at 10
 344 kW·m⁻² with (Figure 8a) and without (Figure 8b) the protective layer at the surface. The in-depth
 345 temperature profile is presented for a series of time steps during the test (i.e. from 0 to 10 min using a time
 346 step of 2.5 min, and from 10 to 30 min using a time step of 5 min). Vertical error bars show the standard
 347 deviation from two repetitions for each thermocouple position. Horizontal error bars indicate the estimated
 348 error in the thermocouple positioning. The results from experiments shown in Figure 8a show good
 349 repeatability, while those presented in Figure 8b show worse repeatability, especially for temperature
 350 measurements near the surface. **This is attributed to the non-uniform thermocouple positioning for repeated**
 351 **experiments, which has a larger impact for measurements near the surface potentially due to the swelling**
 352 **of the material during the thermal decomposition process.**

353 Figure 8a shows a case study where no thermal degradation was observed. Positions close to the
 354 surface achieved a quasi-steady temperature in early stages (from 2.5 min), with a maximum value of 123
 355 °C ± 4 °C. The temperature profile achieved a quasi-steady state after 20-25 min, with a minimal rate of
 356 temperature increase (<1 °C·min⁻¹) for inner positions. **The displacement of the thermal gradient towards**
 357 **higher temperatures for inner positions and with steady temperature at the surface is due to the back-**
 358 **boundary layer. The metallic plate, which acts as a heat sink, was slowly increasing in temperature because**
 359 **the thermal wave had reached the sample back face and, consequently, heat was transferred to the plate.**
 360 The sample section in Figure 8a2 shows that no discolouration was produced in the foam and, consistently,
 361 no release of volatiles was observed during the tests.

362 Figure 8b presents a case study where thermal degradation was observed at the surface of the sample.
 363 Thermal gradients were significantly larger than those shown in Figure 8a1, indicating the clear effect of
 364 the protective layer on the thermal performance. Positions close to the surface achieved a quasi-steady
 365 temperature after 5 min, with a maximum value of $323\text{ °C} \pm 20\text{ °C}$, while the temperature profile again
 366 achieved a quasi-steady state after 20 min, with a minimal rate of temperature increase ($<1\text{ °C}\cdot\text{min}^{-1}$) for
 367 inner positions. Three clear tonalities in the discolouration experienced by the sample can be observed in
 368 the sample section in Figure 8b2. The discolouration is non-uniform, with higher degradation for regions
 369 near the centre-line than near the edge. This indicates that the heat transfer was not behaving perfectly in a
 370 one-dimensional regime. Some cracking can be observed near the surface, where the discolouration is
 371 darker. Additionally, the sample thickness increased by up to 10 mm. A significant release of volatiles was
 372 observed after 3-4 min, but with no ignition during the experiment. Measurements of CO_2 and CO did not
 373 present noticeable concentrations compared to the initial baseline; therefore, these are not presented, which
 374 confirms that no significant oxidation was produced.



375
 376 Figure 8. In-depth thermal profiles of PIRa at $10\text{ kW}\cdot\text{m}^{-2}$ (a1) with and (b1) without protective layer. Centre-
 377 section for the end of the tests (a2, b2).

378 Horizontal error bars: estimated error of $\pm 2\text{ mm}$ in thermocouple positioning.

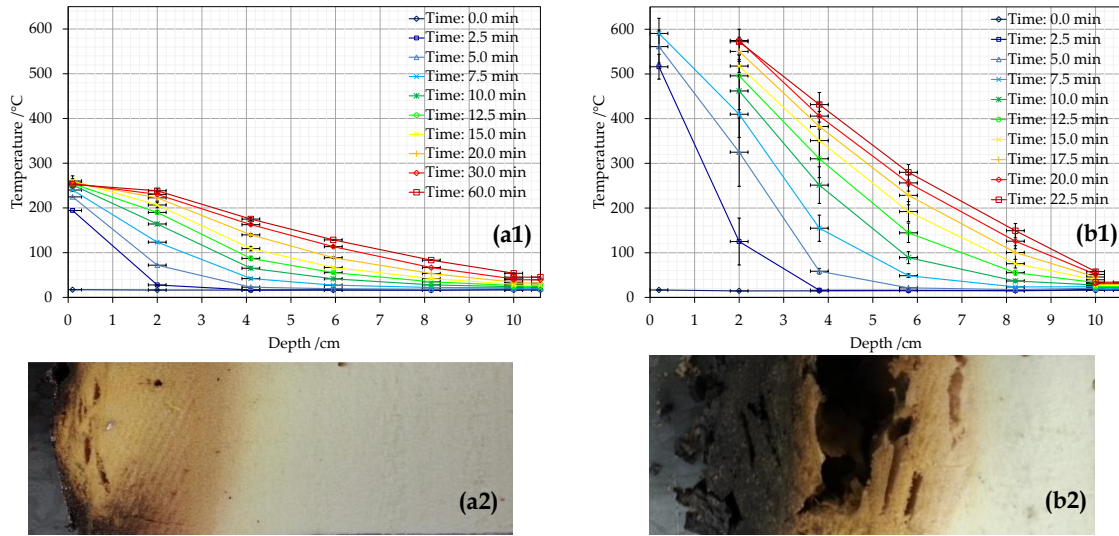
379 Vertical error bars: standard deviation between two repeated tests.

380 Figure 9 shows the in-depth temperature profiles for PIRa experiments tested at $25\text{ kW}\cdot\text{m}^{-2}$ with
 381 (Figure 9a) and without (Figure 9b) the protective layer at the surface. The results from experiments shown
 382 in Figure 9a show good repeatability, with vertical error bars being noticeable only for the surface
 383 thermocouple. The results from experiments shown in Figure 9b, however, present worse repeatability
 384 with the error bars being significantly larger for the three first thermocouples. This non-uniformity is attributed
 385 to the positioning and, more importantly, to the degradation processes forming cracks within the sample

386 and likely different rate of surface oxidation. Significant differences were observed between the
387 performance of the samples with and without the protective layer, which are attributed to the effect that the
388 protective layer has on the radiation absorption due to its low emissivity, and the blocking of air from
389 contact with the surface, thus reducing or cancelling the surface oxidation for those conditions of heating
390 exposure.

391 Figure 9a presents a case study where small thermal degradation was observed. Positions close to the
392 surface achieved a quasi-steady temperature after 2.5-5 min, with a maximum value of $252\text{ }^{\circ}\text{C} \pm 5\text{ }^{\circ}\text{C}$, while
393 the temperature gradient achieved a quasi-steady state after 30 min, with a minimal rate of temperature
394 increase ($<0.5\text{ }^{\circ}\text{C}\cdot\text{min}^{-1}$) for inner positions. Two different tonalities can be observed in the sample section
395 shown in Figure 9a2. This indicates that the heat transfer could be considered as a one-dimensional regime.
396 Small cracks can be observed near the surface. Darker tonalities near the edge of the surface, where the foil
397 ends, might be indicative of an edge effect with lower cooling, therefore presenting higher temperatures.
398 Measurements of carbon dioxide and carbon monoxide did not show concentrations displaced from the
399 baseline, confirming that no oxidation occurred. The sample appeared to have slightly expanded by up to 3
400 mm.

401 Figure 9b shows a case study where severe thermal degradation was observed. Positions close to the
402 surface achieved a maximum temperature of $591\text{ }^{\circ}\text{C} \pm 34\text{ }^{\circ}\text{C}$ at 7.5 min. The lack of measurements from
403 the first thermocouple for the subsequent time steps indicates its detachment from the solid due to
404 consumption of the surrounding material. No steady state was observed for the thermal gradient during the
405 final time steps, with the temperature increasing at a rate of $9\text{-}10\text{ }^{\circ}\text{C}\cdot\text{min}^{-1}$ for inner positions. This rapid rate
406 of temperature change indicates the consumption of material at the surface, thus moving the exposed
407 boundary to lower positions. Three to four tonalities can be observed in the sample section shown in Figure
408 9b2: yellow (virgin material), orange-brown discolouration, and black (char). Small cracks were obtained
409 between the interface of virgin material and orange discolouration, while a series of large cracks can be
410 observed in the brown region, below the char. A thickness regression of approximately 15 mm was
411 obtained, indicating that a significant amount of material was consumed due to surface oxidation.



412
 413 Figure 9. In-depth thermal profiles of PIRa at $25 \text{ kW}\cdot\text{m}^{-2}$ with (a1) and without protective layer (b1). Centre-
 414 section for the end of the tests (a2, b2).

415 Horizontal error bars : estimated error of $\pm 2 \text{ mm}$ in thermocouple positioning.

416 Vertical error bars : standard deviation between two repeated tests .

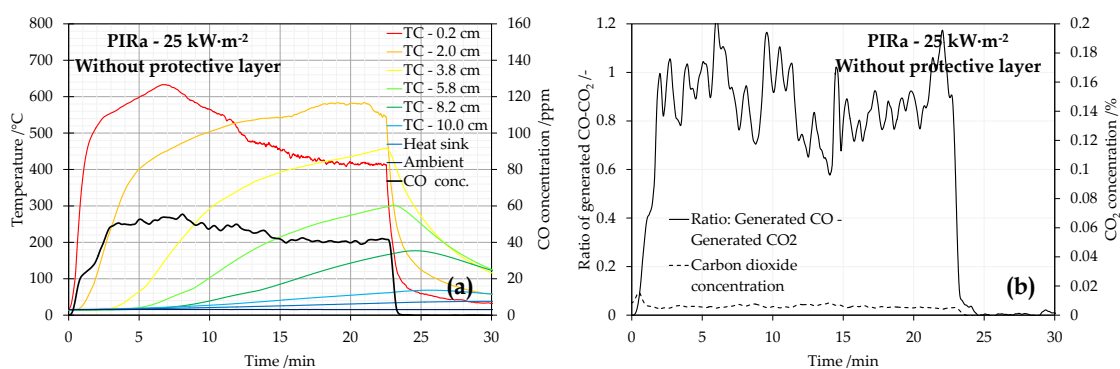
417 Figure 10 shows the sample residue from different perspectives for the test presented in Figure 9b (25
 418 $\text{ kW}\cdot\text{m}^{-2}$ without protective layer for 22.5 min). The surface of the sample presents complex morphology
 419 characterised by craters formed by surface oxidation. It can be observed that the char at the edges and lateral
 420 sides of the sample present a smooth morphology, indicating that oxidation did not take place. This is
 421 consistent with the set-up that uses aluminium foil to prevent air penetration through the sides, thus limiting
 422 oxidation to the top surface.



423
 424 Figure 10. PIRa sample residue at $25 \text{ kW}\cdot\text{m}^{-2}$ without protective layer up to 22.5 minutes (a) Top view (b)
 425 Lateral view (c) Lateral view from section.

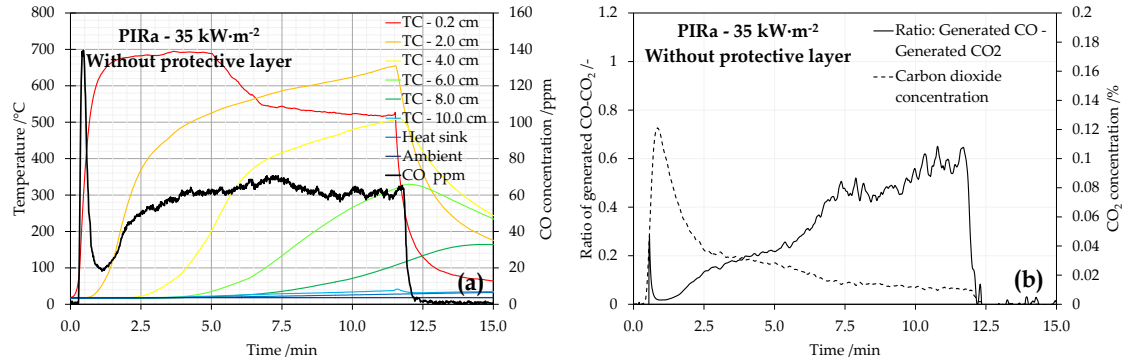
426 A large amount of volatiles were released from the start of the test, shown in Figure 9b and Figure 10,
 427 but ignition was not achieved. Despite the fact that the heat flux used was above the critical heat flux, a
 428 pilot spark was not used. The release of volatiles continued to decrease after one minute. Measurements of
 429 carbon monoxide are presented in Figure 11a with the time-history of temperature measurements. The

430 concentration of CO increased almost from the beginning, probably indicating generation of pyrolysates.
 431 The shape of the CO curve changed slope from 2 to 3 min, and thereafter the CO generation remained
 432 approximately under a steady state during the rest of the test. A slight decrease between 10 and 15 min was
 433 also observed. These measurements are indicative of smouldering combustion (surface oxidation), with a
 434 high CO/CO₂ ratio between 0.8 and 1.2, as shown in Figure 11b. The concentration of CO₂ remained very
 435 low in comparison to the generation of CO₂ presented by flaming of PIR pyrolysates in the previous section.
 436 Additionally, it is shown that the smouldering was not self-sustained since the thermal gradient and CO
 437 generation dropped significantly after the removal of the external heat source. This is due to the closed-cell
 438 structure of the foam that does not allow the free circulation of oxygen through the sample, limiting the
 439 oxidation to the top surface; therefore, the generation of heat is drastically reduced once the external heat
 440 source is removed.



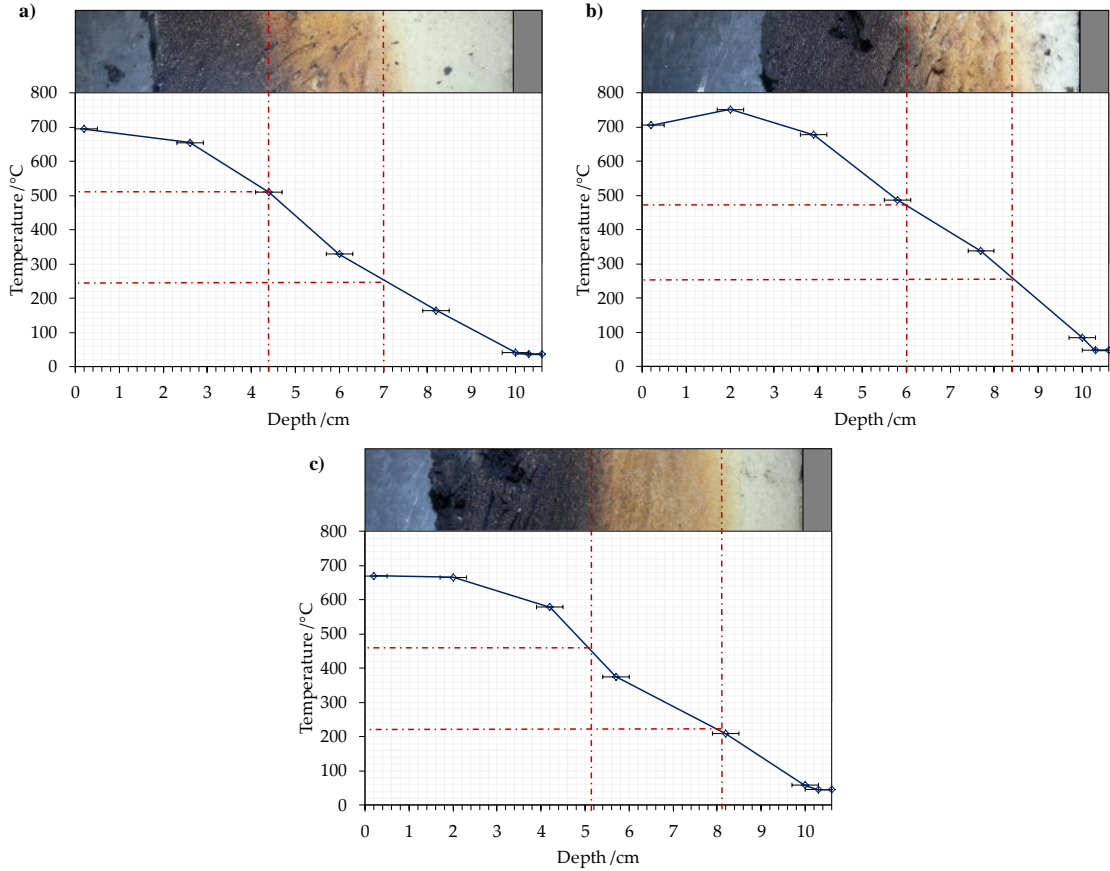
441
 442 Figure 11. Time-history of temperatures within the solid-phase and CO concentration (a) and generated CO
 443 vs generated CO₂ for PIRa with no protective layer at 25 kW·m⁻².

444 A more severe case study is presented in Figure 12, corresponding to a PIRa sample tested at 35 kW·m⁻²
 445 without protective layer. The sample auto-ignited after five seconds of heat exposure, introducing a
 446 different regime that was not observed previously for this experimental series, but for the first series
 447 studying heat release. Figure 12a shows the time-history of temperatures within the solid-phase and the
 448 concentration of generated CO. The thermal evolution within the solid was similar to that presented in
 449 Figure 11a, but with a faster heating rate. The generation of CO followed a different pattern due to flaming
 450 combustion, which was confirmed by the CO₂ concentration presented in Figure 11b. The CO/CO₂ ratio
 451 increased over time, indicating simultaneous flaming and smouldering. This is consistent with the behaviour
 452 presented in previous section.



453
 454 Figure 12. Time-history of temperatures within the solid-phase and CO concentration (a) and generated CO
 455 vs generated CO₂ (b) for PIRa with no protective layer at 35 kW·m⁻².

456 The behaviour from PIRb and PIRc foams was similar to the one presented above. The upper edge of
 457 the temperature envelopes for PIRa, PIRb, and PIRc at 35 kW·m⁻² is presented in Figure 13, with a section
 458 of the sample after the test. The temperature values were interpolated for the interface between the three
 459 main regions of discolouration (yellow, orange-brown and black). In general, the first interface was found
 460 between 220°C and 260°C, while the second interface was identified between 460°C and 520°C. The first
 461 set of temperatures agrees with the value obtained before the onset of the main peak of pyrolysis observed
 462 in differential thermogravimetric (DTG) analyses under nitrogen atmospheres by *Hidalgo et al.* [32, 36].
 463 The second set of temperatures corresponds to the thermal range in which no more significant pyrolysis is
 464 obtained under nitrogen atmospheres. Maximum temperatures measured in the solid-phase, presented
 465 Figure 13, were near 700°C. Thermogravimetric analyses under air atmospheres (50 ml·min⁻¹ flow with
 466 21% of oxygen) showed that the full consumption of mass terminates below 600°C, which indicates that
 467 the diffusion of oxygen then dominates the combustion of char at the surface. However, further assessment
 468 is required to characterise the mechanisms that govern the combustion of this char.



469
 470 Figure 13. Maximum in-depth temperature profile of (a) PIRa, (b) PIRb and (c) PIRc at $35 \text{ kW}\cdot\text{m}^{-2}$ (no protective
 471 layer). Horizontal error bars: estimated error of $\pm 2 \text{ mm}$ in thermocouple positioning.

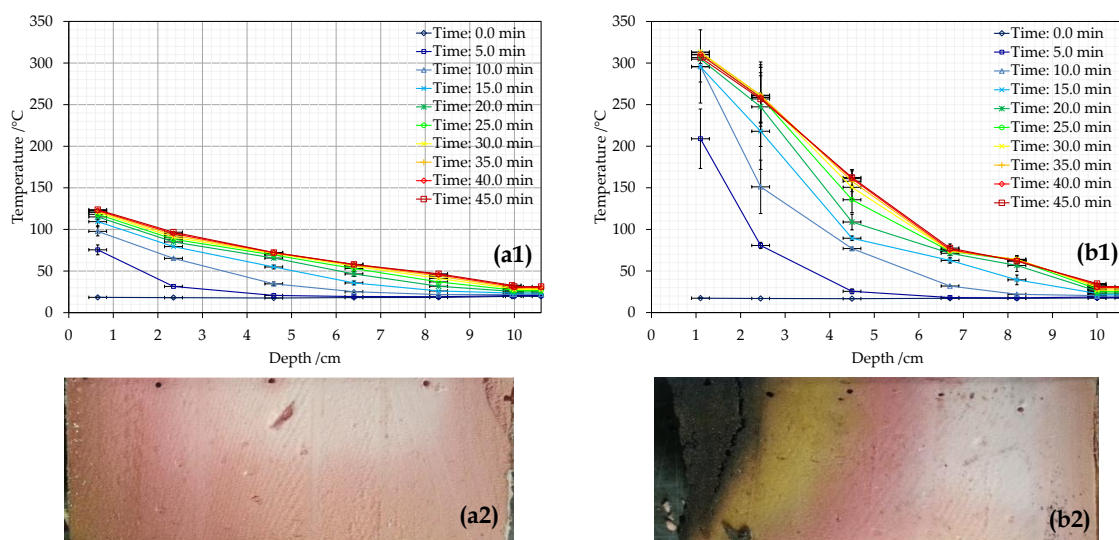
472 4.2.2. Phenolic foam

473 Figure 14 shows the time history of the in-depth temperature profile for PF experiments tested at 10
 474 $\text{kW}\cdot\text{m}^{-2}$ with (Figure 14a) and without (Figure 14b) protective layer at the surface. The results from
 475 experiments shown in Figure 14a present good repeatability in the experiments, while those from
 476 experiments shown in Figure 14b present worse repeatability, especially for temperature measurements
 477 obtained by the two first thermocouples. This is attributed to the non-uniformity of the thermocouple
 478 positioning and especially to the thermal degradation observed, with char being detached from the surface.

479 Figure 14a presents a case study where no clear thermal degradation was observed. Positions close to
 480 the surface achieved a quasi-steady state from 10 min, with a maximum value of $124 \text{ }^\circ\text{C} \pm 1 \text{ }^\circ\text{C}$. The
 481 temperature profile achieved a quasi-steady state from 15-20 min, with a minimal rate of temperature
 482 increase ($<1^\circ\text{C}\cdot\text{min}^{-1}$) for inner positions. A change in the slope of the thermal profile was obtained near
 483 the second thermocouple once the steady state was achieved. The sample section displayed in Figure 14a2
 484 shows that some discolouration of a darker pink tonality was produced near the surface. Additionally, the

485 sides and bottom of the section have different tonality than the centre, which indicates that material suffers
 486 from oxidation at ambient temperatures. No release of volatiles was observed during the tests.

487 Figure 14b presents a case study where clear thermal degradation was observed at the surface of the
 488 sample. Thermal gradients were significantly larger than the ones shown in Figure 14a, indicating the clear
 489 effect of the protective layer on the thermal performance again. The temperature close to the surface
 490 achieved a quasi-steady state after 10 min, with a maximum value of $296\text{ }^{\circ}\text{C} \pm 44\text{ }^{\circ}\text{C}$ at this time step. The
 491 temperature profile achieved a quasi-steady state from 25 min, with a minimal rate of temperature increase
 492 ($<1^{\circ}\text{C}\cdot\text{min}^{-1}$) for inner positions. The in-depth temperature profile during the steady-state shows an
 493 interesting shape, with two different slopes converging at $78\text{ }^{\circ}\text{C}$, indicating temperature dependency of the
 494 thermal properties and/or endothermic processes at lower temperatures. This is consistent with the change
 495 of slope observed in Figure 14a. Four clear tonalities in the discolouration experienced by the material can
 496 be observed in the sample section shown in Figure 14b2. The degradation seems to be non-uniform, with
 497 higher degradation for regions near the centre-line than near the edge. This indicates that the heat transfer
 498 was not behaving perfectly as a one-dimensional regime. Cracks and delamination can be observed within
 499 the first 20 mm from the surface, in the char area, as shown in Figure 17a. Delamination is probably due to
 500 spalling from the sample; popping and snapping sounds could be heard during the experiment. No
 501 significant surface regression or oxidation was observed, but measurements of carbon dioxide and carbon
 502 monoxide indicated low concentrations compared to the initial baseline. This is indicative of minor
 503 oxidation from the delaminated pieces.



504
 505 Figure 14. In-depth thermal profiles of PF at $10\text{ kW}\cdot\text{m}^{-2}$ with (a1) and without protective layer (b1). Centre-
 506 section for the end of the tests (a2, b2).

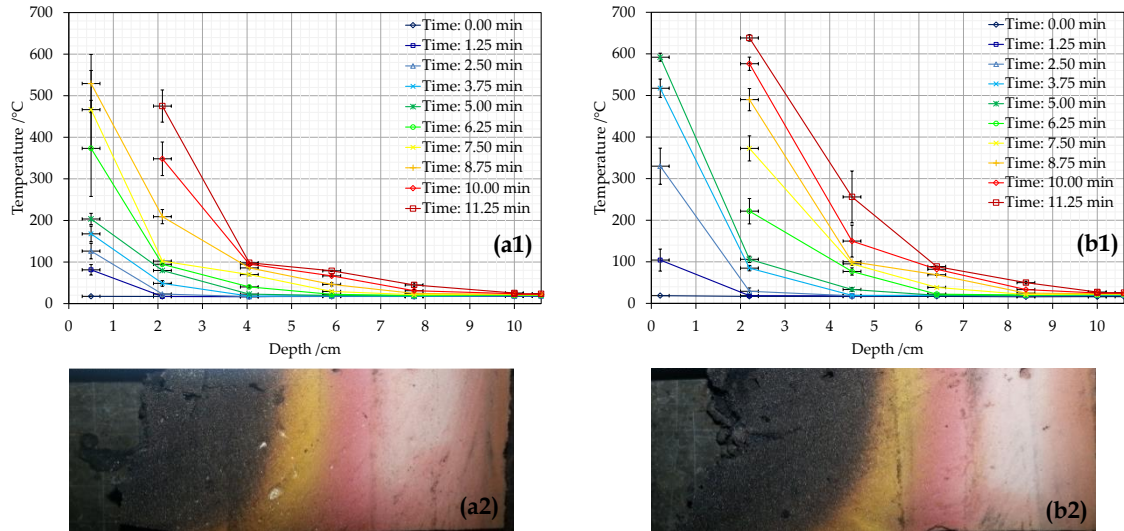
507 Horizontal error bars : estimated error of ± 2 mm in thermocouple positioning.

508 Vertical error bars : standard deviation between two repeated tests .

509 Figure 15 shows the in-depth temperature profiles for PF experiments tested at $25 \text{ kW} \cdot \text{m}^{-2}$ with (Figure
510 15a) and without (Figure 15b) the protective layer at the surface. The results shown in Figure 15a and Figure
511 15b present good repeatability except for the first thermocouples. Slightly better performance was observed
512 for the samples with a protective layer (Figure 15a) than those without (Figure 15b), with lower thermal
513 gradients for same times of exposure. However, the protective layer did not prevent the onset of thermal
514 degradation.

515 Figure 15a presents a case study where the effectiveness of the protective layer was lost after certain
516 temperature and thermal degradation was eventually achieved. The temperature profile close to the surface
517 showed a moderate rate of temperature increase around $30\text{-}50 \text{ }^\circ\text{C} \cdot \text{min}^{-1}$ until 5 min, achieving a temperature
518 of $204 \text{ }^\circ\text{C} \pm 14 \text{ }^\circ\text{C}$, at which point the rate of increase rose significantly since the protective layer started to
519 detach and lift after 4 min of heat exposure. As a result, the temperature near the surface achieved a
520 maximum value below $600 \text{ }^\circ\text{C}$ at around 9 min, when the thermocouple detached from the initial position
521 due to consumption of the surrounding material. Approximately 20 mm of material was consumed by the
522 end of the tests. Four different uniform tonalities can be observed in the sample section between the edge
523 and the centre-line, as shown in Figure 15a2, indicating that the heat transfer could be considered essentially
524 as a one-dimensional regime. No cracks within the core of the sample were obtained, but the top of the
525 sample presented a rough surface with some random cracks. Measurements of carbon dioxide and carbon
526 monoxide showed concentrations displaced from initial baseline, confirming the occurrence of solid-phase
527 oxidation. For simplicity, these results are not presented herein, but for the case shown in Figure 15b which
528 is equivalent.

529 Figure 15b shows a case study where severe thermal degradation was observed from early times in the
530 test (2.5 min). The temperature close to the surface achieved a maximum value of $592 \text{ }^\circ\text{C} \pm 10 \text{ }^\circ\text{C}$ at 5 min.
531 No steady state was observed for the thermal gradient during the final time steps, with the temperature
532 increasing with a rate of $9\text{-}10 \text{ }^\circ\text{C} \cdot \text{min}^{-1}$ for inner positions. This rate was only observed for positions with a
533 temperature higher than $100 \text{ }^\circ\text{C}$, indicating a clear endothermic effect at that temperature range. A high rate
534 of temperature increase, without achieving the steady-state, indicates the consumption of material at the
535 surface, thus moving the exposed boundary to lower positions. The thermal degradation experienced was
536 similar to that shown in Figure 15a. The surface of the material is presented in Figure 17c, showing crater
537 morphology on the edges and rough surface and random long cracks expanding from the centre to the edges.



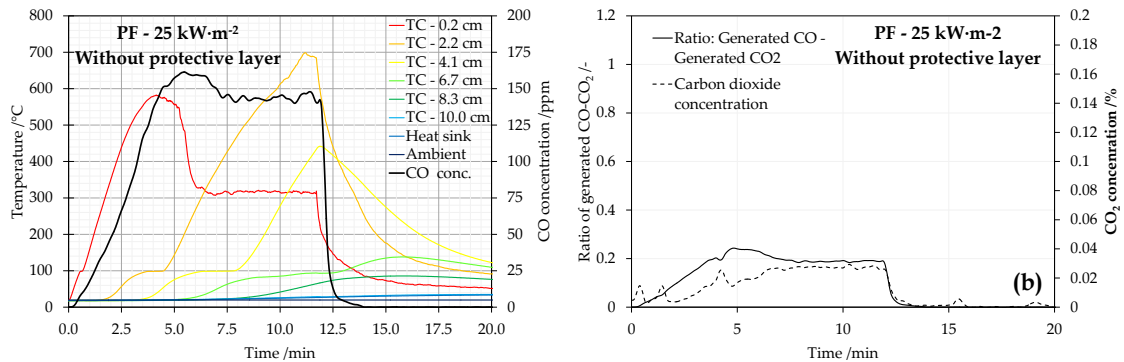
538

539 Figure 15. In-depth thermal profiles of PF at $25 \text{ kW}\cdot\text{m}^{-2}$ with (a1) and without protective layer (b1). Centre-
 540 section for the end of the tests (a2, b2).

541 Horizontal error bars: estimated error of $\pm 2 \text{ mm}$ in thermocouple positioning.

542 Vertical error bars: standard deviation between two repeated tests.

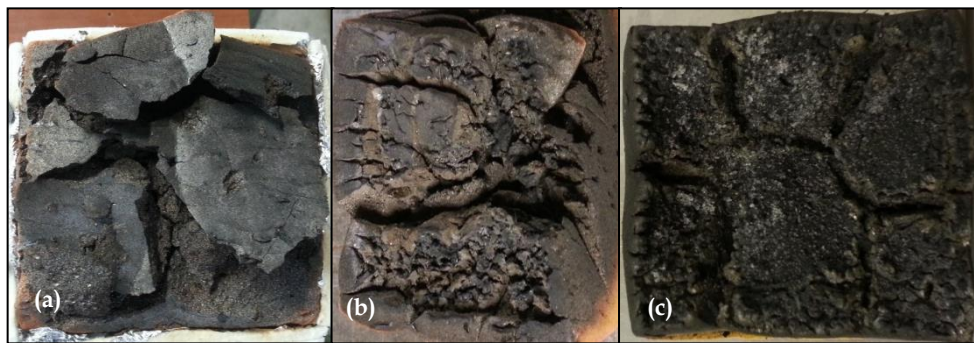
543 Measurements of carbon monoxide are presented in Figure 16a with the time-history of temperature
 544 measurements. The concentration of CO increased until 5 min, when it achieved a steady state at around
 545 150 ppm. These measurements are indicative of smouldering combustion (surface oxidation), suggesting a
 546 constant rate of oxidation. Similarly, the CO/CO₂ ratio increased until 5 min as shown in Figure 16b,
 547 remaining approximately constant at around 0.2. The concentration of CO₂ remained very low in
 548 comparison to the generation of CO₂ presented for the flaming of PF in previous sections. Additionally, it
 549 is shown that the smouldering was not self-sustained since the thermal gradient and CO generation dropped
 550 significantly after removing the external heat source. This is due to the closed-cell structure of the foam
 551 that does not allow the free circulation of oxygen through the sample. Additionally, a plateau of
 552 temperatures was clearly observed below 100°C in Figure 16a, indicating an endothermic reaction,
 553 probably due to water desorption in the polymer.



554

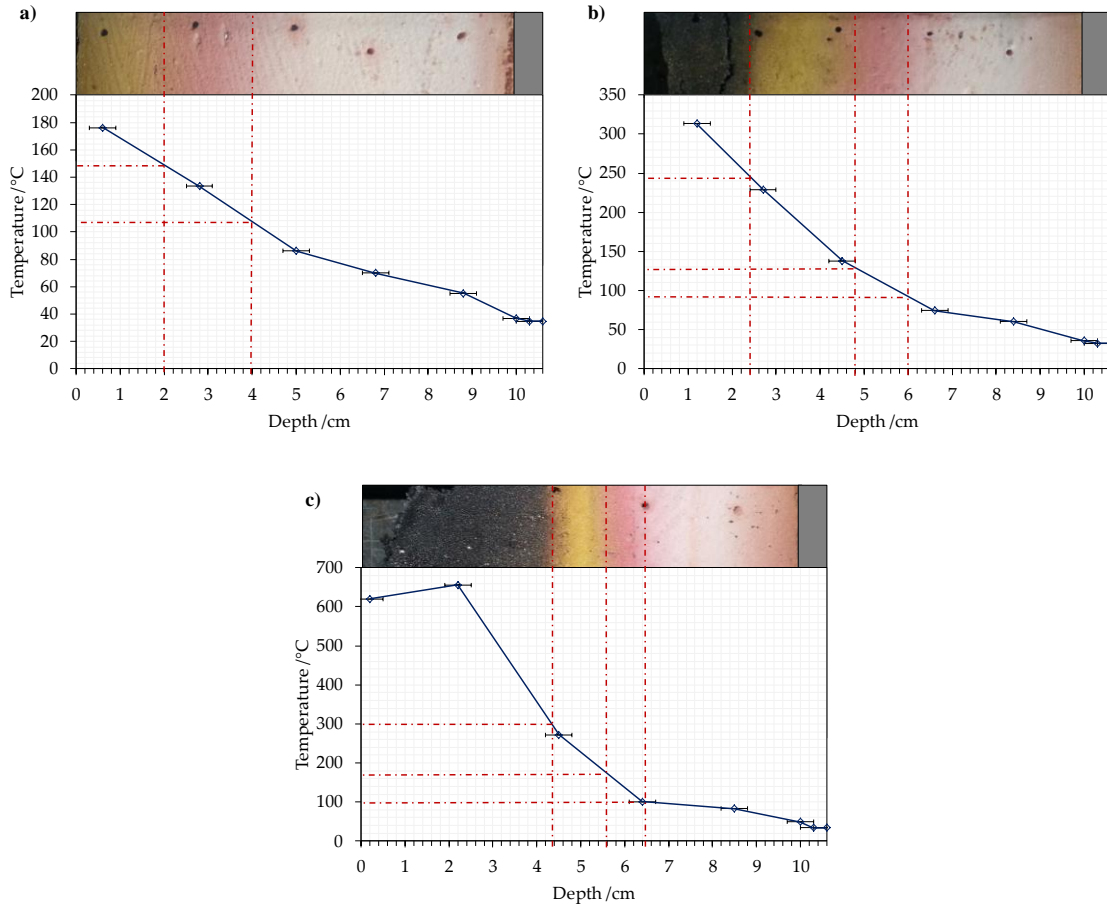
555 Figure 16. Time-history of temperatures within the solid-phase and CO concentration (a) and generated CO
556 vs. generated CO₂ (b) for PF without protective layer at 25 kW·m⁻².

557 Images from the surface of the remaining residue for PF experiments without the protective layer at
558 10, 15 and 25 kW·m⁻² are shown in Figure 17. Different patterns indicate the significance of surface
559 oxidation. Figure 17a shows the occurrence of the delamination effect when the achieved temperatures are
560 not high enough to trigger the oxidation of the char created. Figure 17b shows that the oxidation at the
561 surface is not homogenous, indicating the high complexity of the oxidation mechanism, while Figure 17c
562 shows the case of a smouldering process with relatively constant rate of surface regression as shown in
563 Figure 16.



564
565 Figure 17. PF sample residue at 10 kW·m⁻² (a), 15 kW·m⁻² (b) and 25 kW·m⁻² (c) without protective layer.

566 The upper edge of the temperature envelopes for different experiments are presented separately in
567 Figure 18, together with a section of the sample after the test. **Temperatures values were interpolated for**
568 **the interface between the three main regions of discolouration (light pink, dark pink, orange-brown and**
569 **black). In general, the first interface, which was observed as a plateau of temperature in Figure 18a, was**
570 **around 100 °C, near the change of slope in the thermal gradient. The second interface was identified**
571 **between 125 °C and 160 °C, which agrees with the temperature before the first peak of pyrolysis observed**
572 **in differential thermogravimetric (DTG) analyses under nitrogen atmospheres in [32, 36]. The third**
573 **interface was identified between 250 °C and 300 °C, which agrees with the temperature between the first**
574 **and second peak of pyrolysis observed in DTG analyses under nitrogen atmospheres. Maximum**
575 **temperatures measured in the solid-phase and shown Figure 18 were between 600 °C and 700 °C, while**
576 **TGA analyses under air atmospheres showed that all mass consumption ends below 600°C in an air**
577 **atmosphere. This indicates that the diffusion of oxygen probably dominates the combustion of char at the**
578 **surface.**



579

580

581 Figure 18. Maximum in-depth temperature profile of PF: a) $15 \text{ kW}\cdot\text{m}^{-2}$ (foil) b) $10 \text{ kW}\cdot\text{m}^{-2}$ (no foil) c) $25 \text{ kW}\cdot\text{m}^{-2}$
 582 (no foil) Horizontal error bars: estimated error of $\pm 2 \text{ mm}$ in thermocouple positioning.

583 5. Summary

584 This paper has presented the results from two experimental programmes based on ad-hoc Cone
 585 Calorimeter tests. This work aimed to investigate the fire performance of charring closed-cell polymeric
 586 insulation materials, specifically polyisocyanurate (PIR) and phenolic foam (PF), so that a comprehensive
 587 protocol can be set for assessing the evolution of hazard imposed by the material. The first experimental
 588 programme macroscopically analysed the fire performance of these foams by studying heat release rate,
 589 mass loss and gas species. The second programme mapped the thermal degradation processes in relation to
 590 temperature measurements within the solid-phase, correlating the evolution of the thermal profile
 591 experienced by the material to previous results obtained by thermogravimetry.

592 The first series of experiments was based on 100 mm thick samples tested using the Cone Calorimeter
 593 (with spark igniter) and reproducing levels of irradiation from the critical heat flux up to $65 \text{ kW}\cdot\text{m}^{-2}$.
 594 Calorimetry calculations for PIR and PF samples showed the typical shape obtained from charring
 595 materials. A peak of heat release rate per unit area (HRRPUA) between $120\text{-}170 \text{ kW}\cdot\text{m}^{-2}$ was observed for

596 PIR, with a decay below $60 \text{ kW}\cdot\text{m}^{-2}$ represented by the formation of a char layer and the transition of the
597 pyrolysis front towards inner depths. The peak heat release rate per unit area for PF was observed to be in
598 the range $80\text{-}140 \text{ kW}\cdot\text{m}^{-2}$, with a decay and subsequent increase or decrease depending on the external heat
599 flux. Despite its larger critical heat flux for ignition, PF showed larger mass loss and surface regression for
600 the same conditions of heat exposure after a certain time. This is attributed to the overlapping of pyrolysis
601 and char oxidation reactions in a close temperature range for PF, while PIR presents clearly separated
602 temperature ranges for the pyrolysis and char oxidation reactions. The effective heat of combustion for PIR
603 was found to be in the range of $13\text{-}21 \text{ kJ}\cdot\text{g}^{-1}$, while for PF the range was $15\text{-}21 \text{ kJ}\cdot\text{g}^{-1}$. Complimentary gas
604 analyses demonstrated different regimes of combustion for PIR and PF, i.e. flaming at the surface with a
605 CO/CO₂ ratio **between 0.05 and 0.10 for PIR**, and between 0.025 and 0.05 for PF, followed in both cases
606 by smouldering of the char left at the surface, with intermittent flaming at sides and an increasing
607 CO/CO₂ ratio as flaming was reduced. These phenomena may occur simultaneously, depending on the
608 displacement speed of the pyrolysis front and the oxidation rate at the surface.

609 The second series of experiments was primarily concerned with understanding the thermal evolution
610 and dynamics of the thermal degradation experienced by PIR and PF. This stage was based on 100 mm
611 thick samples tested with the Cone Calorimeter (without spark igniter), and reproducing heating scenarios
612 with different severities. Measurements of temperature within the insulation allowed mapping of the
613 different thermal degradation processes, which were previously identified by thermogravimetric
614 techniques. Measurements of gas species (carbon monoxide, carbon dioxide and oxygen) were also taken
615 to determine whether oxidation processes occurred, i.e. flaming from the pyrolysis gases or smouldering
616 from the char generated after pyrolysis.

617 A technique based on comparing the eventual thermal discolouration through the thickness of a sample
618 was correlated to the upper edge of the temperature envelopes during the test and the thermogravimetric
619 results. Three clear domains were observed in the thermal evolution of PIR and PF, corresponding to the
620 virgin material, pyrolysis region, and char. Polyisocyanurate was found to expand in the regions where it
621 was pyrolysing, creating a series of cracks or gaps within the structure of the foam. Phenolic foam, however,
622 spalled, probably due to the loss of chemically bound water, which was evidenced by plateaus of
623 temperature around 100°C . A clear effect was observed in the thermal performance of the rigid foams such
624 as PIR and PF when samples were tested with the protective layer attached to the exposed surface. This is
625 related to the reduction of the fraction of absorbed heat flux due to the low emissivity of the protective
626 layer, as well as other effects such as the reduction in the rate of oxidation, via avoiding the contact of
627 oxygen with the charred material or the inhibition of a good mixing between air and pyrolysates.

628 While the pyrolysis was clearly governed by the thermal evolution of the solid-phase for these charring
629 materials, the rate of oxidation was identified as a diffusion-controlled mechanism. Indeed, values of
630 temperature higher than those obtained by thermogravimetry under air conditions were observed within the
631 char. The rate of oxidation of the char was also found to be governed by the external heat flux, which also
632 determined the evolution of the pyrolysis front. The smouldering process of the char remaining after
633 pyrolysis from PIR and PF was found to self-extinguish after the external heat source was removed. This
634 indicates that the generated heat from the char oxidation at the surface, with the particular heat losses
635 obtained for the tested conditions, was not sufficient to sustain the process. Additionally, the closed-cell
636 structure does not allow the diffusion of air through the foam, thus limiting the smouldering.

637 Further work should focus on modelling tasks to characterise the thermal behaviour and pyrolysis of
638 these materials. Additionally, the mechanism of char oxidation should be further investigated.

639 Acknowledgements

640 The authors would like to gratefully acknowledge funding contribution from Rockwool International A/S
641 towards sponsoring the Ph.D. studies for Juan P. Hidalgo. Michal Krajcovic and Alastair Bartlett are
642 gratefully acknowledged for their precious lab assistance on the performed experimental programmes.

643 References

- 644 1. A.M. Papadopoulos, *State of the art in thermal insulation materials and aims for future developments*,
645 *Energy and Buildings*, vol. 37, no. 1, pp. 77–86, doi:10.1016/j.enbuild.2004.05.006, 2005.
- 646 2. A. Fangareggi, and L. Bertucelli, *Thermoset insulation materials in appliances, buildings and other*
647 *applications* in *Thermosets: Structure, Properties and Applications*, pp. 254-288,
648 doi:10.1533/9780857097637.2.254, 2012.
- 649 3. EU. *Directive 2010/31/EU of the European Parliament and of the Council of 19 May 2010 on the*
650 *energy performance of buildings*, *Official Journal of the European Union*, pp. 13–35,
651 doi:10.3000/17252555.L_2010.153.eng, 2010.
- 652 4. U. Krause, W. Grosshandler, and L. Gritzso, *The International FORUM of Fire Research Directors: A*
653 *position paper on sustainability and fire safety*, *Fire Safety Journal*, vol. 49, pp. 79-81,
654 doi:10.1016/j.firesaf.2012.01.003, 2012.
- 655 5. B. Meacham, B. Poole, J. Echeverria, and R. Cheng, *Fire Safety Challenges of Green Buildings*,
656 Springer New York, doi:10.1007/978-1-4614-8142-3, 2012.

- 657 6. J.M. Buist, S.J. Grayson, and W.D Woolley, *Fire and Cellular Polymers*, doi:10.1007/978-94-009-
658 3443-6, 1987.
- 659 7. C. Dick, E. Dominguez-Rosado, B. Eling, J.J. Liggat, C.I. Lindsay, S.C. Martin, M.H. Mohammed, G.
660 Seeley, and C.E. Snape, *The flammability of urethane-modified polyisocyanurates and its relationship*
661 *to thermal degradation chemistry*, *Polymer*, vol. 42(3), pp. 913-923, doi:10.1016/s0032-
662 3861(00)00470-5, 2001.
- 663 8. E. Dominguez-Rosado, J.J. Liggat, C.E. Snape, B. Eling, and J. Pitchel, *Thermal degradation of*
664 *urethane modified polyisocyanurate foams based on aliphatic and aromatic polyester polyol*, *Polymer*
665 *Degradation and Stability*, vol. 78(1), pp.1-5, doi:10.1016/S0141-3910(02)00086-1, 2002.
- 666 9. I. Vitkauskienė, R. Makuška, U. Stirna, and U. Cabulis, *Thermal Properties of Polyurethane-*
667 *Polyisocyanurate Foams Based on Poly (ethylene terephthalate) Waste*, *Materials Science*, vol. 17(3),
668 doi:10.5755/j01.ms.17.3.588, 2011.
- 669 10. T.R. Hull, and B.K. Kandola, *Retardancy of Polymers: New Strategies and Mechanisms*, doi:
670 10.1039/9781847559210, 2009.
- 671 11. A.A. Stec, and T.R. Hull, *Assessment of the fire toxicity of building insulation materials*, *Energy and*
672 *Buildings*, vol. 43, no. 2-3, pp. 498-506, doi: doi:10.1016/j.enbuild.2010.10.015, 2011.
- 673 12. M. Smolka, and Y. Suurenbroek, *Smoke and heat emissions as measures for interaction of tested*
674 *elements with test environment in fire resistance testing* in *Proceedings of the 13th International*
675 *Interflam Conference*, 2013.
- 676 13. K.T. Paul, *Burning characteristics of materials*, *Fire and Materials*, vol. 3(4), pp. 223-231,
677 doi:10.1002/fam.810030408, 1979.
- 678 14. K.T. Paul, *Characterization of the burning behaviour of polymeric materials*, *Fire and Materials*, vol.
679 8(3), pp. 137-147, doi:10.1002/fam.810080304, 1984.
- 680 15. J.M. Buist, S.J. Grayson, and W.D. Woolley, *Fire and Cellular Polymers*, doi:10.1007/978-94-009-
681 3443-6, 1987.
- 682 16. M.J. Scudamore, P.J. Briggs, and F.H. Prager, *Cone calorimetry – a review of tests carried out on*
683 *plastics for the association of plastic manufacturers in Europe*, *Fire and Materials*, vol. 15(2), pp. 65-
684 84, doi:10.1002/fam.810150205, 1991.
- 685 17. T.G. Cleary, and J.G. Quintiere, *NISTIR 4664. Flammability Characterization of Foam Plastics*,
686 *National Institute of Standards and Technology*, 1991.

- 687 18. M. Modesti, A. Lorenzetti, F. Simioni, and M. Checchin, *Influence of different flame retardants on fire*
688 *behaviour of modified PIR/PUR polymers*, *Polymer Degradation and Stability*, vol.74(3), pp. 475-479,
689 doi:10.1016/S0141-3910(01)00171-9, 2001.
- 690 19. A. Tewarson, and R.F. Pion, *Flammability of plastics—I. Burning intensity*, *Combustion and Flame*,
691 vol. 26, pp. 85-103, doi:10.1016/0010-2180(76)90059-6, 1976.
- 692 20. M. Modesti, and A. Lotenzetti, *Improvement on fire behaviour of water blown PIR–PUR foams: use of*
693 *an halogen-free flame retardant*, *European Polymer Journal*, vol.39(2), pp. 263-268,
694 doi:10.1016/S0014-3057(02)00198-2, 2003.
- 695 21. A.P. Mouritz, and A.G. Gibson, *Fire Properties of Polymer Composite Materials*, Springer, 2006
- 696 22. M.L. Auad, L. Zhao, H. Shen, S.R. Nutt, and U. Sorathia, *Flammability properties and mechanical*
697 *performance of epoxy modified phenolic foams*, *Journal of Applied Polymer Science*, vol. 105(3), pp.
698 1399-1407, doi: 10.1002/app.24405, 2007.
- 699 23. W.D. Woolley, *Are Foams a Fire Hazard?* in *Fire and cellular polymers*, pp. 61–75, doi:10.1007/978-
700 94-009-3443-6_3, 1986.
- 701 24. D. Drysdale, *Fundamentals of the fire behaviour of cellular polymers*, *Fire and Cellular Polymers*, pp.
702 61-75, doi:10.1007/978-94-009-3443-6_4, 1986.
- 703 25. P. J. Briggs, *Fire Behaviour of Rigid Foam Insulation Boards* in *Fire and cellular polymers*, pp. 117–
704 133, doi:10.1007/978-94-009-3443-6_8, 1986.
- 705 26. V. Brannigan, *The regulation of technological innovation: the special problem of fire safety standards*,
706 *FireSeat "Fire & Building Safety in the Single European Market"*, pp. 20-33
- 707 27. ASTM D2863. *Measuring the minimum oxygen concentration to support candle-like combustion of*
708 *plastics (oxygen index)*, ASTM International, West Conshohocken, PA, 2013.
- 709 28. BS ISO 5660-1. *Reaction-to-fire tests. Heat release, smoke production and mass loss rate. Heat release*
710 *rate (cone calorimeter method) and smoke production rate (dynamic measurement)*, BSI, 2015.
- 711 29. ASTM E1321. *Standard Test Method for Determining Material Ignition and Flame Spread Properties*,
712 ASTM International, West Conshohocken, PA, 2013.
- 713 30. J.P. Hidalgo, S. Welch, and J.L. Torero, *Performance criteria for the fire safe use of thermal insulation*
714 *in buildings*, *Construction and Building Materials*, vol. 100, pp. 285-297,
715 doi:10.1016/j.conbuildmat.2015.10.014, 2015.

- 716 31. J.P. Hidalgo, S. Welch, and J.L. Torero, *Design tool for the definition of thermal barriers for*
717 *combustible insulation materials*, Proceedings of the 2nd IAFSS European Symposium of Fire Safety
718 Science, ISBN 978-9963-2177-0-0, 2015.
- 719 32. J.P. Hidalgo, J.L. Torero, and S. Welch, *Experimental characterisation of the fire behaviour of thermal*
720 *insulation materials for a performance-based design methodology*, Fire Technology (in press),
721 doi:10.1007/s10694-016-0625-z, 2017.
- 722 33. J.P. Hidalgo, N. Gerasimov, R.M. Hadden, J.L. Torero, and S. Welch, *Methodology for estimating*
723 *pyrolysis rates of charring insulation materials using experimental temperature measurements*, Journal
724 of Building Engineering, vol. 8, pp. 249-259, doi: 10.1016/j.job.2016.09.007, 2016.
- 725 34. BS EN 13501-1. Fire classification of construction products and building elements. Part 1:
726 Classification using data from reaction to fire tests, 2009.
- 727 35. BS EN 1363-1. Fire resistance tests - Part 1: General Requirements, 2012.
- 728 36. J.P. Hidalgo, *Performance-Based Methodology for the Fire Safe Design of Insulation Materials in*
729 *Energy Efficient Buildings*, Ph.D. Thesis, The University of Edinburgh,
730 <http://hdl.handle.net/1842/10601>, 2015.
- 731 37. S. Quinn, *Chemical blowing agents: providing production, economic and physical improvements to a*
732 *wide range of polymers*, Plastics, Additives and Compounding, vol. 3. pp. 16–21, doi:10.1016/S1464-
733 391X(01)80162-8, 2001.
- 734 38. R. Carvel, T. Steinhaus, G. Rein, and J.L. Torero, *Determination of the flammability properties of*
735 *polymeric materials: A novel method*, Polymer Degradation and Stability, vol. 96, no. 3, pp. 314–319,
736 doi:10.1016/j.polyimdegradstab.2010.08.010, 2011.
- 737 39. J. V. Beck, *Thermocouple Temperature Disturbances in Low Conductivity Materials*, Journal of Heat
738 Transfer, vol. 84, no. 2, pp. 124, doi:10.1115/1.3684310, 1962.
- 739 40. P. Reszka, *In-Depth Temperature Profiles in Pyrolyzing Wood*, Ph.D. thesis, The University of
740 Edinburgh, <http://hdl.handle.net/1842/2602>, 2008.
- 741 41. W.M. Thornton, *The relation of oxygen to the heat of combustion of organic compounds*, Philosophical
742 Magazine Series, vol. 33, pp. 196–203, 1917.
- 743 42. A. Tewarson, *Generation of Heat and Chemical Compounds in Fires*, in SFPE Handbook of Fire
744 Protection Engineering, 3rd ed., P.J. DiNunno, D. Drysdale, C.L. Beyler, W.D. Walton, R.L.P. Custer,
745 and J.M. Watts, Eds. Massachusetts, U.S.A.: National Fire Protection Association, 2002.

- 746 43. M.L. Janssens, *Measuring rate of heat release by oxygen consumption*, Fire Technology, vol. 27, no.
747 3, pp. 234–249, doi:10.1007/BF01038449, 1991.
- 748 44. H. Biteau, T. Steinhaus, C. Schemel, A. Simeoni, G. Marlair, N. Bal, and J. Torero, *Calculation*
749 *Methods for the Heat Release Rate of Materials of Unknown Composition*, Fire Safety Science, vol. 9,
750 pp. 1165–1176, doi:10.3801/IAFSS.FSS.9-1165, 2008.